Journal of Power Sources 213 (2012) 128–139

Contents lists available at SciVerse ScienceDirect

Journal of Power Sources

journal homepage: www.elsevier.com/locate/jpowsour

Effects of Al- and Mn-contents in the negative MH alloy on the self-discharge and long-term storage properties of Ni/MH battery

L. Kong [a,b], B. Chen [a], K. Young [c,*], J. Koch [c], A. Chan [c], W. Li [b]

[a] School of Metallurgical Science and Engineering, Central South University, Changsha, Hunan, China
[b] Shenzhen Highpower Technology Co., LTD, Luoshan Industrial Zone, Pinghu, Longgang, Shenzhen, Guangdong, China
[c] Ovonic Battery Company, 2983 Waterview Drive, Rochester Hills, MI 48309, USA

ARTICLE INFO

Article history:
Received 7 February 2012
Received in revised form
30 March 2012
Accepted 31 March 2012
Available online 24 April 2012

Keywords:
Hydrogen absorbing materials
Transition metal alloys
Metal hydride electrode
Electrochemical reactions
Nickel metal hydride battery

ABSTRACT

The charge retention and long-term storage properties of AB_5-based Ni/MH batteries were studied by partial/complete replacements of Al- and Mn-contents by Ni in the AB_5 alloys, separately. A high-temperature accelerated testing scheme (60 °C and 60-days) was proven to be capable of predicting the status of batteries after long-term storages at room temperature (6-months and 293-days). Charge retention and impedance measured from the accelerated scheme can be correlated to the open-circuit voltage and impedance after long-term storage, respectively. While both Al and Mn were important to maintain good charge retention, Al, with its good oxidation resistance to slow down the oxidation/corrosion of the MH alloy, contributed to a lower internal impedance, Mn, on the other hand, slowed down the pulverization rate and reduced the irreversible capacity loss, however, contributed to a higher reversible capacity loss. The addition of Y_2O_3 in the positive electrode was found to raise the open-circuit voltage and reduce both reversible capacity loss and impedance increase during long period storage by slowing down the oxidation/corrosion of the MH alloy in the negative electrode.

1. Introduction

Ni/metal hydride rechargeable (Ni/MH) batteries have been widely used in consumer, propulsion, and stationary applications. Recently, both the self-discharge and long-term storage characteristics of Ni/MH batteries have drawn a lot of attention in the industry [1–5]. While the former is important to offer a ready-to-use rechargeable battery that can replace disposable primary alkaline batteries, the latter is important to emerging energy storage markets. Both properties are strongly related to the other. During storage, the capacity of the Ni/MH battery decreases. While part of the capacity loss is reversible due to self-discharge, other parts of the loss are not. Many mechanisms of self-discharge have been discussed before, such as redox shuttling from multi-valence nitrogen [6–10], soluble cations from metal hydride (MH) alloy in the negative electrode [2,11–16], micro-shorts caused by deposits formed in the separator [2,17], hydrogen consumption in the negative electrode [18–21], and oxygen evolution from the positive electrode. The irreversible capacity loss can be attributed to the dissolution of the surface CoOOH conducting network [22,23], the corrosion/passivation of negative electrode [8,18,24], the decomposition of positive electrode [22] and separator [22], and the poisoning of the positive electrode from cations originated from the negative electrode [12,14,22]. It seems like the overall composition in the hydrogen storage alloy as well as the active material in the negative electrode can play a key role in both reversible and irreversible capacity loss. Hence, a much closer look at the effects of compositional change on capacity loss is necessary.

In a typical chemical composition of AB_5-based MH alloy suitable for Ni/MH applications, Al and Mn are the elements with the highest solubilities in the KOH electrolyte [25]. The leached out Al and Mn cations migrate and deposit onto the surface of the positive electrode [8,12,14], which can cause pre-maturing of oxygen evolution and consequently lower charge efficiency. Al and Mn influence the process of self-discharge in two different ways: while the redox shuttling between Mn (II) and Mn (III) can cause a dramatic increase in self-discharge [14], Al retards oxidation of the negative electrode [4], thus reducing self-discharge [26]. Similarly, the effects of Al and Mn on storage are also different. Shinyama and his coworkers reported on the effects of Al and Mn on the positive electrode by adding them in the electrolyte and found that Al increased the internal impedance by 6% and reduced the surface area by 10% while Mn did not change either measure significantly [12]. Although some preliminary information is available for the role of Al and Mn in the charge retention and long-

* Corresponding author. Tel.: +1 248 293 7000; fax: +1 248 299 4520.
E-mail address: kwoyoung@yahoo.com (K. Young).

0378-7753/$ – see front matter © 2012 Elsevier B.V. All rights reserved.
doi:10.1016/j.jpowsour.2012.03.099

Table 1
Design compositions and ICP results in atomic percentage of 7 alloys.

Alloy #	La	Ce	Pr	Nd	Ni	Co	Mn	Al	Comments
1	10.5	4.3	0.5	1.3	61.3	12.0	6.6	3.4	Base
ICP	10.2	4.1	0.4	1.2	61.6	12.5	6.7	3.4	
2	10.5	4.3	0.5	1.3	62.6	12.0	6.6	2.1	67% Al
ICP	10.4	4.3	0.5	1.3	62.8	12.0	6.6	2.0	
3	10.5	4.3	0.5	1.3	63.6	12.0	6.6	1.1	33% Al
ICP	10.7	4.3	0.5	1.3	63.6	11.7	6.8	1.2	
4	10.5	4.3	0.5	1.3	64.7	12.0	6.6	0.0	0% Al
ICP	10.6	4.4	0.5	1.3	64.2	12.2	6.8	0.0	
5	10.5	4.3	0.5	1.3	63.5	12.0	4.4	3.4	67% Mn
ICP	10.6	4.3	0.5	1.3	63.2	12.2	4.5	3.4	
6	10.5	4.3	0.5	1.3	65.7	12.0	2.2	3.4	33% Mn
ICP	10.6	4.4	0.5	1.3	65.3	12.2	2.2	3.5	
7	10.5	4.3	0.5	1.3	67.9	12.0	0.0	3.4	0% Mn
ICP	10.7	4.3	0.5	1.3	67.7	12.2	0.1	3.4	

term storage, a final determination can be made only through a thorough study with compositional variations in the MH alloy, a study that is presented here.

2. Experimental setup

Ingots were prepared in a 2 kg induction furnace from raw materials in elemental form in a MgO crucible. The melt was poured into a steel pancake-shape mold through an alumina tundish. The ingot was annealed at 960 °C for 8-h in vacuum. The chemical composition of each sample was examined by a Varian *Liberty* 100 inductively-coupled plasma (ICP) system. A Philips *X'Pert Pro* X-ray diffractometer (XRD) was used to study the micro structure, and a JEOL-*JSM6400* scanning electron microscopy (SEM) with energy dispersive spectroscopy (EDS) capability was used to study the phase distribution and composition. PCT characteristics for each sample were measured using a Suzuki-Shokan multi-channel PCT system. In the PCT analysis, each sample was first activated by a 2-h

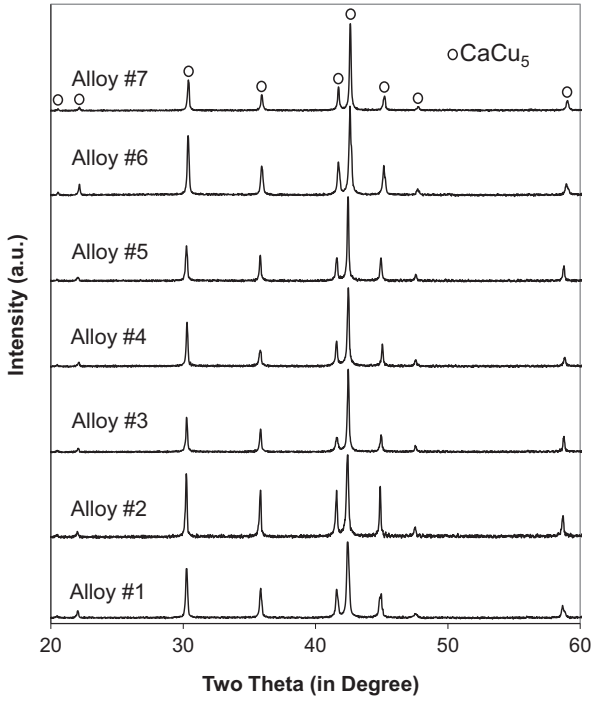

Fig. 1. XRD patterns using Cu-K_α as the radiation source for alloys #1 to #7. All peaks can be fit into a $CaCu_5$ structure.

Table 2
Summary of XRD results.

Alloy #	*a* (Å)	*c* (Å)	*c*/*a*	Unit cell volume (Å^3)	(001)-FWHM (°)	Crystallite size (Å)
1	5.0183	4.0437	0.8058	88.19	0.143	758 (63)
2	5.0158	4.0391	0.8053	88.00	0.160	612 (45)
3	5.0111	4.0326	0.8047	87.70	0.146	596 (44)
4	5.0136	4.0235	0.8025	87.59	0.174	635 (49)
5	5.0134	4.0339	0.8046	87.81	0.231	710 (64)
6	5.0032	4.0231	0.8041	87.21	0.188	626 (50)
7	4.9964	4.0111	0.8028	86.72	0.151	607 (46)

thermal cycle between 300 °C and room temperature at 25 atm H_2 pressure. The PCT isotherms at 30 °C and 45 °C were then measured. Details of both electrode and cell preparations as well as measurement methods have been reported previously [27,28]. The annealed ingots were ground into −200 mesh size and made into negative electrode. AAA-size Ni/MH batteries were assembled to evaluate the self-discharge and long-term storage properties. The substrates used in the positive and negative electrodes were foamed Ni gauze and Ni-plated punched steel strip, respectively. In preparing the positive electrode, $Ni(OH)_2$ and CoO powders were mixed with 1% PTFE and pasted onto the substrate. Additional 0%, 2%, and 4% Y_2O_3 powder (>99.5% purity, D50 = 5 microns) were added in the paste. In preparing the negative electrode, MH alloy powder, SBR, graphite, Ni powder and water were mixed into slurry and pasted onto the substrate. Then, the positive electrode, the negative electrode, and separator were rolled and sealed into a steel can coated on the inside with Ni. The negative-to-positive capacity ratio was around 1.7. The internal impedance was tested by using BK-300 (Guangzhou Blue-key electronic industry Co., Ltd) in the AC mode with the test frequency set at 1000 ± 100 Hz.

3. Results

Seven alloys with varying amounts of Al and Mn were prepared— the designed compositions are shown in Table 1. The Al-reduction series was composed of alloys #1 (base), #2 (67% Al compared to the Al-content in the base alloy), #3 (33% Al), and #4 (0% Al) while the Mn-reduction series consisted of alloys #1 (base),

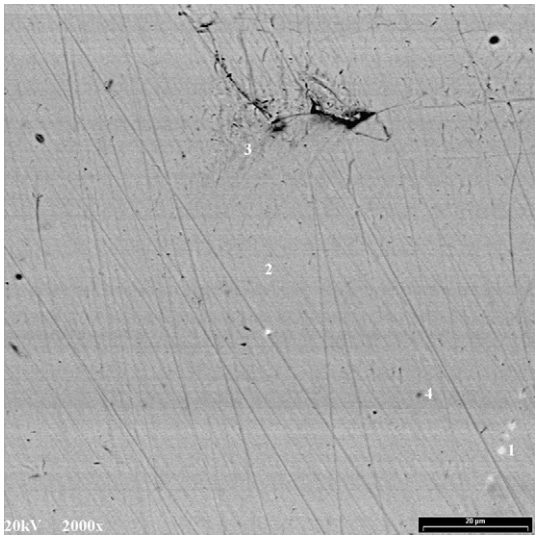

Fig. 2. SEM backscattering electron image from alloy #5. The compositions measured by EDS in areas identified by numbers are listed in Table 3.

Table 3
EDS results of areas identified in the SEM micrograph of alloy #5 (Fig. 2).

Area #	La	Ce	Pr	Nd	Ni	Co	Mn	Al
1	10.3	4.7	0.0	0.9	64.4	11.9	4.8	3.1
2	10.3	4.7	0.0	0.8	64.6	11.8	4.9	3.0
3	10.3	4.7	0.0	0.8	64.9	11.8	4.7	2.9
4	10.2	4.6	0.0	0.9	65.0	12.1	4.7	2.5
Entire	10.3	4.5	0.0	0.9	64.3	11.9	4.8	3.3

#5 (67% Mn compared to the Mn-content in the base alloy), #6 (33% Mn), and #7 (0% Mn). Ni-contents in both series were increased to compensate for the reductions in Al and Mn. ICP results from the annealed samples are listed in Table 1 and show very close compositions to the designed values.

3.1. Micro structure analysis

The XRD patterns of the 7 alloys are shown in Fig. 1. All the peaks can be fit into a $CaCu_5$ structure. Part of the peak intensity variation is due to the preferential occupation sites for Mn in the $CaCu_5$ structure [29,30]. The unit cell information collected from XRD patterns is included in Table 2. Both lattice constants *a* and *c* of the base alloy (#1) were larger than those of the other alloys that have lower Al- and Mn-contents because of the relative larger atomic size of Al and Mn as compared to Ni. The *c*/*a* ratios decreased as the Al- and Mn-contents reduced, suggesting a higher degree of pulverization during the hydride/dehydride cycling [31]. The unit cells became smaller as the Al- and Mn-contents were reduced; therefore, higher equilibrium pressures are expected [32]. Although the size difference between Al/Ni is larger than that between Mn/Ni, the Al-series alloys still have larger unit cell volumes than those from Mn-series due to the smaller amount of Al/Ni replacement in the Al-series. The full-width at half maximum of the $CaCu_5$ (001) diffraction peak and the crystallite size calculated from the whole pattern fitting using Bragg-Brentano model with JADE 9 software are listed in Table 2. The base alloy had the narrowest diffraction peak and corresponded to the largest crystallite size. Reductions in Al- and Mn-contents were shown to reduce the crystallite size.

The micro structures for these alloys were studied by SEM. Samples were mounted and polished in epoxy blocks, rinsed and dried before entering the SEM chamber. After annealing, no secondary phases were observed in all seven alloys. A representative backscattering electron image (BEI) from alloy #5 is presented in Fig. 2. The compositions in several areas of Alloy #5 with various contrasts (identified numerically in the micrographs) were studied using EDS, and the results are listed in Table 3. All EDS compositions were very close to the average values except for small variations in Al-content. The EDS and ICP results differed slightly, especially in Mn- and Al-contents. ICP, being a wet chemistry method, is essentially a bulk analysis tool with exceptional accuracy, small minimum detection limits, and frequent calibrations. EDS in electron microscopy, on the other hand, depends on the calculation of the k-factor, which considers both X-ray emission and absorption in a defined volume; the results are consistent but not as accurate as those of ICP. Judging from XRD and SEM/EDS results, the reductions in Al- and Mn-contents in the alloy did not create new phases.

Table 4
Summary of gaseous phase hydrogen storage properties.

Alloy #	PCT capacity (%)	Pressure @ 0.6% (MPa)	Hysteresis @ 0.6%	$-\Delta H$ (kJ mol^{-1})	$-\Delta S$ (J mol^{-1}K^{-1})
1	1.32	0.024	0.06	35	103
2	1.38	0.032	0.08	35	104
3	1.44	0.043	0.10	36	111
4	1.46	0.056	0.10	36	113
5	1.34	0.039	0.09	36	110
6	1.39	0.075	0.08	36	117
7	1.37	0.190	0.10	36	122

3.2. Gaseous phase hydrogen storage study

The gaseous phase hydrogen storage properties of the alloys were studied using PCT. The resulting absorption and desorption isotherms measured at 30 °C are shown in Fig. 3. The information obtained from the PCT study is summarized in Table 4. The storage capacities increased with the reductions in both Al and Mn. The equilibrium plateau pressure, defined as the mid-point of the desorption isotherm, increased as the Ni-content increased in both the Al- and Mn-reduction series, which agrees with the shrinking unit cells observed from XRD analysis. The hysteresis of the PCT

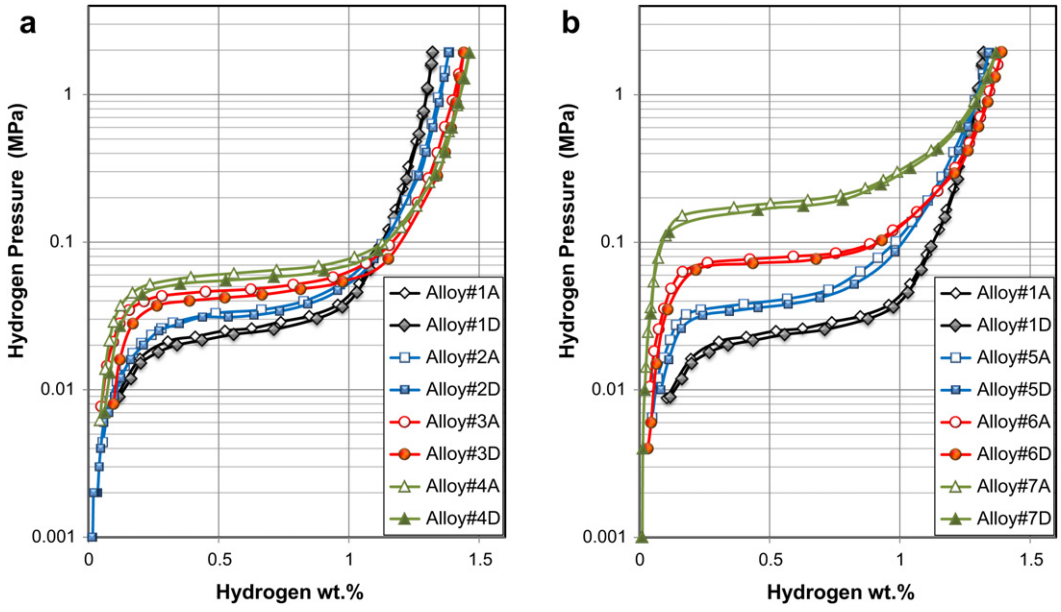

Fig. 3. PCT isotherms of alloys alloy #1–4 (a) and alloy #1 and #5–7 (b) measured at 30 °C. Open and solid symbols are for absorption and desorption curves, respectively.

Table 5
ICP results of the solutions from alloys #1-7 after etching in 30% KOH for 4 h. All numbers are in ppm.

Alloy #	Al	Co	Mn	La
1	28.4	0.7	0.1	0.1
2	22.2	0.9	0.4	ND
3	16.2	1.1	0.8	ND
4	ND	1.3	1.1	ND
5	24.6	0.7	0.3	ND
6	23.3	0.2	0.1	ND
7	19.5	ND	ND	ND

isotherm, listed in Table 4, is defined as $\ln(P_a/P_d)$, where P_a and P_d are the absorption and desorption equilibrium plateau pressures, respectively. The hysteresis can be used to predict the pulverization rate of the alloy during cycling [33–35]. Alloys with reduced Al and Mn showed slightly larger PCT hysteresis, suggesting a higher degree of pulverization, a result which is consistent with the reduced c/a ratios found in XRD analysis.

Desorption equilibrium plateau pressure measured at different temperatures were used to calculate the changes in enthalpy (ΔH) and entropy (ΔS) by the equation

$$\Delta G = \Delta H - T\Delta S = RT\ln P \quad (1)$$

where R is the ideal gas constant and T is the absolute temperature. The results of these calculations are listed in Table 4. The ΔH values of hydride formation were very similar, which indicates similar hydrogen-metal bond strengths among all alloys. Compared to the rather stable ΔH values, ΔS became lower and closer to the entropy difference between the hydrogen gas and hydrogen in solid [36] as the Al- and Mn- contents were reduced, which indicates a higher degree of completion of an ordered hydride structure.

3.3. Hot alkaline etching

In order to study the corrosion behavior of these MH alloys, hot alkaline etching was performed with 30% KOH at 100 °C for 4 h. Similar etching experiment was conduct before comparing AB_2, AB_5, and A_2B_7 MH alloys [37]. The concentrations of various metal components in the resultant solutes were measured by ICP, and the results are listed in Table 5. Al had the highest solubility and was followed by Co and Mn at about the same level. As the Al-content reduced in the Al-series, more Co and Mn dissolved into the solution, which indicates the corrosion resistance nature of Al. Lower Mn-content seems to reduce corrosion judging from the reduced amounts of Al and Co leached out from the MH alloy surface. The concentration of La leached out from the MH alloy is small in alloy #1 and under the detection level of ICP for each of the rest of the alloys.

3.4. Battery formation

After being assembled and sealed, the batteries went through formation cycles. They were first kept at room temperature for 20 h, and then the temperature was raised to 45 °C and maintained for 28 h. The first formation cycle was performed with the following sequence of charges and discharges: a 0.05C charge for 3 h, a 0.2C charge for 4 h, a 0.5C discharge for 80 min, a 0.2C charge for 5 h, a 0.5C discharge for 80 min, and a 0.2C discharge to a cut-off voltage at 1.0 V. The second formation cycle was performed with: a 0.2C charge for 6 h, a 0.5C discharge for 80 min, and a 0.2C discharge to a cut-off voltage at 1.0 V. The third and fourth formation cycles employed the same steps: a 0.2C charge for 7 h, a 0.5C discharge to 1.0 V followed by a 0.2C discharge to 1.0 V.

For the initial capacity measurement, batteries were charged with a 0.2C rate for 7 h and rested for 30 min, followed by a 0.2C discharge to 1.0 V. Since the battery capacity was limited by the positive electrode, the capacities within each group were about the same. Groups with higher levels of Y_2O_3 additive showed slightly lower capacities. Two important cell parameters, the initial open-circuit voltage (OCV) and internal impedance were tracked during the entire charge retention experiment. During storage, OCV has to stay at a relative high level to prevent the dissociation of CoOOH onto the surface of charged $Ni(OH)_2$ powder and also to protect the negative electrode from oxidation. The internal impedance can be used as an indication of the loss of the CoOOH conductive network

Table 6
Summary of test results from AAA batteries made from 7 alloys.

Positive	Alloy#	Initial		After 60-day at 60 °C				Room Temp 6-months		Room Temp 293-days	
		OCV	Imp., mΩ	OCV	Imp., mΩ	Charge retention, % retention	Charge recovery, %	OCV	Imp., mΩ	OCV	Imp., mΩ
0% Y_2O_3	1	1.394	33.2	1.261	45.9	47.7	97.7	1.2774	34.9	1.270	36.5
0% Y_2O_3	2	1.408	34.0	1.265	72.1	32.3	91.2	1.2861	41.4	1.273	42.3
0% Y_2O_3	3	1.411	36.6	1.251	151.6	32.5	93.3	1.2872	79.9	1.280	100.3
0% Y_2O_3	4	1.412	36.7	1.247	133.1	13.4	94.0	1.2891	81.6	1.282	101.6
0% Y_2O_3	5	1.410	35.2	1.265	70.3	21.2	90.1	1.2880	40.2	1.281	42.8
0% Y_2O_3	6	1.420	37.1	1.268	57.7	11.2	88.6	1.2941	36.6	1.287	38.2
0% Y_2O_3	7	1.428	37.2	1.246	45.1	3.1	81.7	1.2996	29.8	1.290	31.3
2% Y_2O_3	1	1.398	29.9	1.251	31.7	65.1	95.7	1.2862	30.5	1.276	31.1
2% Y_2O_3	2	1.412	32.2	1.257	41.7	47.6	92.9	1.2920	34.2	1.281	35.0
2% Y_2O_3	3	1.415	34.3	1.257	73.6	27.8	91.9	1.2930	44.6	1.282	48.5
2% Y_2O_3	4	1.415	33.4	1.258	71.2	19.0	92.1	1.2928	50.0	1.283	55.8
2% Y_2O_3	5	1.415	32.2	1.257	33.8	46.7	91.2	1.2932	31.9	1.283	32.5
2% Y_2O_3	6	1.421	32.2	1.264	34.9	30.4	90.1	1.2960	30.6	1.287	31.2
2% Y_2O_3	7	1.428	32.6	1.260	31.9	9.1	86.7	1.2998	28.6	1.292	29.4
4% Y_2O_3	1	1.396	31.2	1.250	33.5	64.7	97.7	1.2840	31.2	1.274	31.7
4% Y_2O_3	2	1.406	31.7	1.256	43.7	48.5	93.1	1.2906	35.6	1.281	36.6
4% Y_2O_3	3	1.411	33.7	1.250	63.3	33.7	94.5	1.2918	46.1	1.282	50.9
4% Y_2O_3	4	1.410	33.1	1.246	70.5	22.6	92.0	1.2922	49.5	1.283	55.0
4% Y_2O_3	5	1.409	31.8	1.256	38.7	47.1	91.6	1.2918	33.8	1.282	34.7
4% Y_2O_3	6	1.418	32.6	1.259	35.4	31.5	89.8	1.2960	29.7	1.288	30.3
4% Y_2O_3	7	1.426	32.7	1.251	34.3	10.5	89.7	1.2996	27.7	1.292	28.5

in the positive electrode and passivation on the negative electrode surface. The initial values of OCV and impedance were measured with a 0.2C charge for 7 h and a 30 min rest for the three groups of alloys with different amounts of Y_2O_3 additives and are listed in the third and fourth columns in Table 6. In general, OCVs in the 2% Y_2O_3 group were higher than those from the other two groups. The impedances were lower for the cells with higher Y_2O_3-contents. Within each group, both OCV and impedance went up with an increase in Ni-content. The Mn-reduction series had higher OCVs and impedances than the Al-reduction series did.

3.5. Charge retention

The charge retention characteristics of the batteries were studied with an accelerated scheme at a higher temperature, which is a standard test procedure used in the industry to shorten the test period. Batteries were put into a 60 °C oven, and both OCV and impedance were measured on a weekly basis. After 60-days in the oven, the OCV and impedance were measured and are listed in the fifth and sixth columns in Table 6. These batteries were then discharged at a 0.2C rate to 1.0 V, and the remaining capacities were recorded and are listed in the seventh columns as charge retention. These batteries were cycled three times with a 7-h 0.2C charge and a 0.2C discharge to 1.0 V. Capacities were averaged and listed in the eighth column as charge recovery.

After cells were stored at 60 °C for 60-days, the OCV for every cell dropped about 150 mV. The group with higher Y_2O_3-content had a slightly lower OCV on average. In 0% Y_2O_3 group of cells, the base alloy showed the highest OCV with the lowest one being the Mn-free alloy. In other two groups, the variations in OCV are less obvious. In impedance, all cells except alloy #7 with 2% Y_2O_3 additive showed increases. The averaged increase in the 0% Y_2O_3 group was higher than those from other two groups. Within each group, the increases in the Al-reduction series were higher than those in the Mn-reduction series.

The remaining capacities (charge retention) after the cells were stored at 60 °C for 60-days are plotted in Fig. 4a. The reductions in charge retention for both Al- and Mn-series were about the same and clearly show that Y_2O_3 is beneficial in maintaining higher charge retention. The averaged capacity from three cycles after storage (charge recovery) is plotted in Fig. 4b. The irreversible capacity losses were different from one another. Cells made from the base alloy showed the best charge recovery and the degradation in the Al-reduction series was less severe than in the Mn-reduction series. The effect of Y_2O_3 on charge recovery is not as obvious. The reversible capacity loss during storage can be obtained by subtracting charge recovery from charge retention; these values are plotted in Fig. 4c. The reversible capacity loss in all series increased with the decreases in Al- and Mn-contents. Except for the middle two alloys in the Mn-series that show higher reversible capacity loss than those from Al-series with 0% Y_2O_3, alloys show similar results at the same percentage of Al- or Mn-reduction when compared within the groups of 0%, 2%, and 4% Y_2O_3. From the same figure, one can also conclude that the addition of Y_2O_3 in the positive electrode lowered the reversible capacity loss during storage.

After the capacity measurement, cells in the first group (0% Y_2O_3) were cut in the middle and mounted onto an epoxy block for cross-section SEM study for the purpose of investigating the deposits in the separator. EDS mapping was performed with a Thermo Noran System 7. The findings are summarized in Table 7, and representative elemental mappings for alloys #1, #3, and #7 are shown in Figs. 5–7, respectively. In the cell made from the base alloy, large amounts of oxides of Mn, Co, Fe, and Al were trapped in the separator, and oxides of Mn, Co, and Fe were also found at the

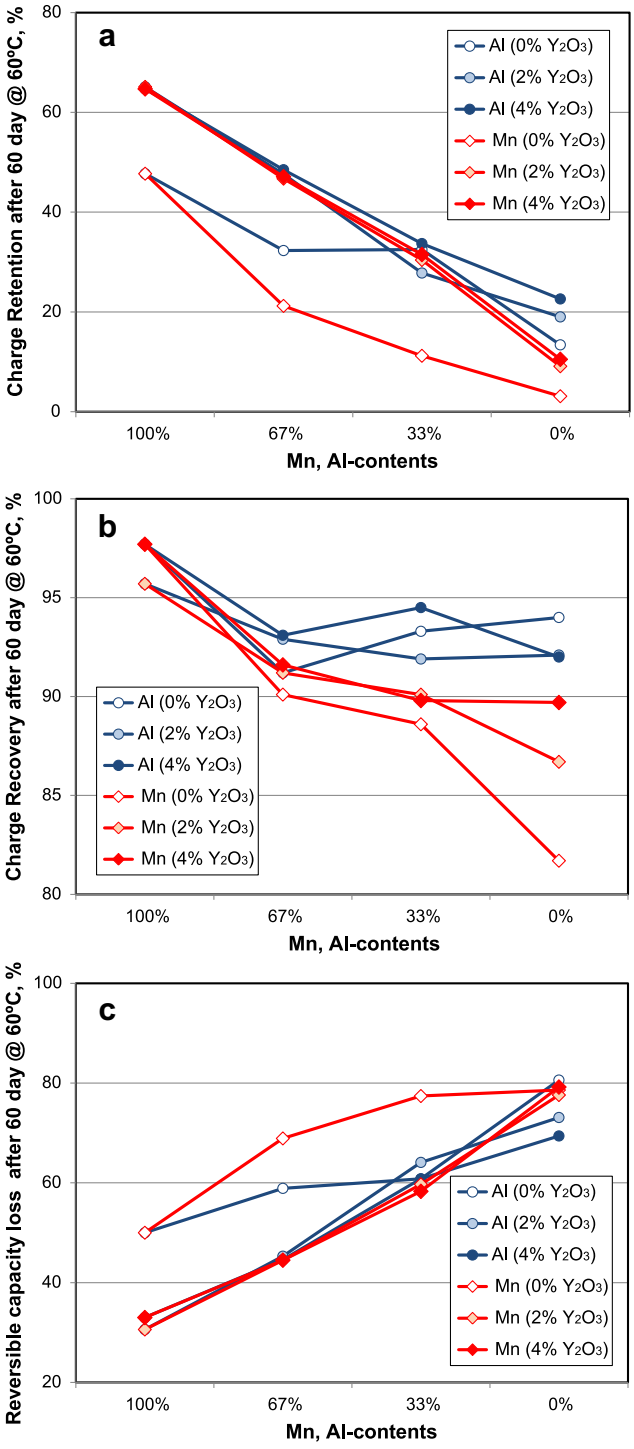

Fig. 4. The plots of charge retention (a), charge recovery (b), and reversible capacity loss (c) of batteries against the composition after 60-days storage at 60 °C.

interface between the separator and the positive electrode. Fe was found in both the negative and positive electrodes while Zn from the positive electrode and Al from the negative electrode migrated onto opposing electrodes. The presence of Fe is attributed to the negative electrode substrate, tab, and can, which were made from Ni-plated stainless steel and were exposed after the plating corroded. In the Al-series, as the Al-content decreased, Ni and Zn started to appear in the separator, thus indicating that the disintegration of the positive electrode was occurring. In addition, the

Table 7
Summary of observations from EDS mapping of alloys with 0% Y_2O_3 after 60-days at 60 °C storage.

Alloy #	In separator	Separator/positive interface	Negative electrode	Positive electrode
1 (100%)	Mn, Co, Fe, Al, O	Mn, Co, Fe, O	Fe, Zn	Al, Fe
2 (66% Al)	Mn, Ni, Zn, Fe, O	Mn	Fe, Zn	Al, Fe
3 (33% Al)	Ni, Zn, Fe, O	None	Fe, Zn	Al, Fe
4 (0% Al)	Mn, Co, Fe, Ni, Zn, O	None	Fe, Zn	Mn, Fe
5 (66% Mn)	Ni, Zn, Fe, Al, O	Mn, Fe, O	Fe, Zn	Al, Fe
6 (33% Mn)	Al, O	Mn, Fe, O	Fe, Zn	Al, Fe
7 (0% Mn)	Al, O	None	Fe, Zn	Al, Fe

interface between separator and positive electrode became cleaner; the negative electrode stayed the same; and, as expected, the amount of Al in the positive electrode decreased. In the Mn-series, as Mn-content decreased, the observed Mn deposits in the separator were reduced while aluminum oxide remained, and Mn/Fe oxide deposits at the separator/positive electrode interface were reduced while the contaminations in negative and positive electrodes remain unchanged.

In order to further study the distribution of corrosion product qualitatively, Soxhlet extraction (24 h) was performed on the

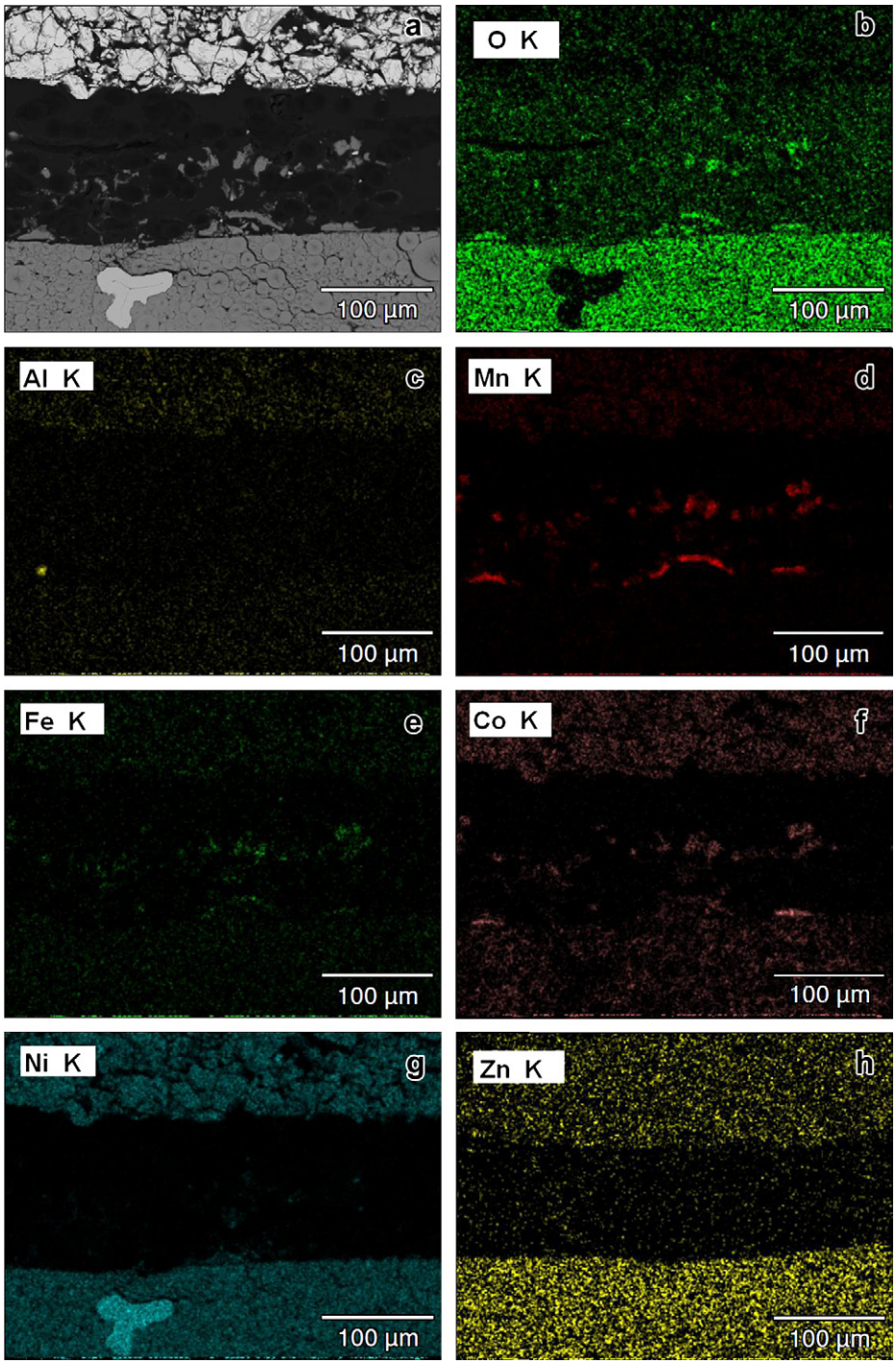

Fig. 5. SEM backscattering electron image (a) and EDS elemental mappings of O (b), Al (c), Mn (d), Fe (e), Co (f), Ni (g), and Zn (h) from the battery made from alloy #1 after 60-days storage at 60 °C. Positive electrode is at the bottom of the micrograph.

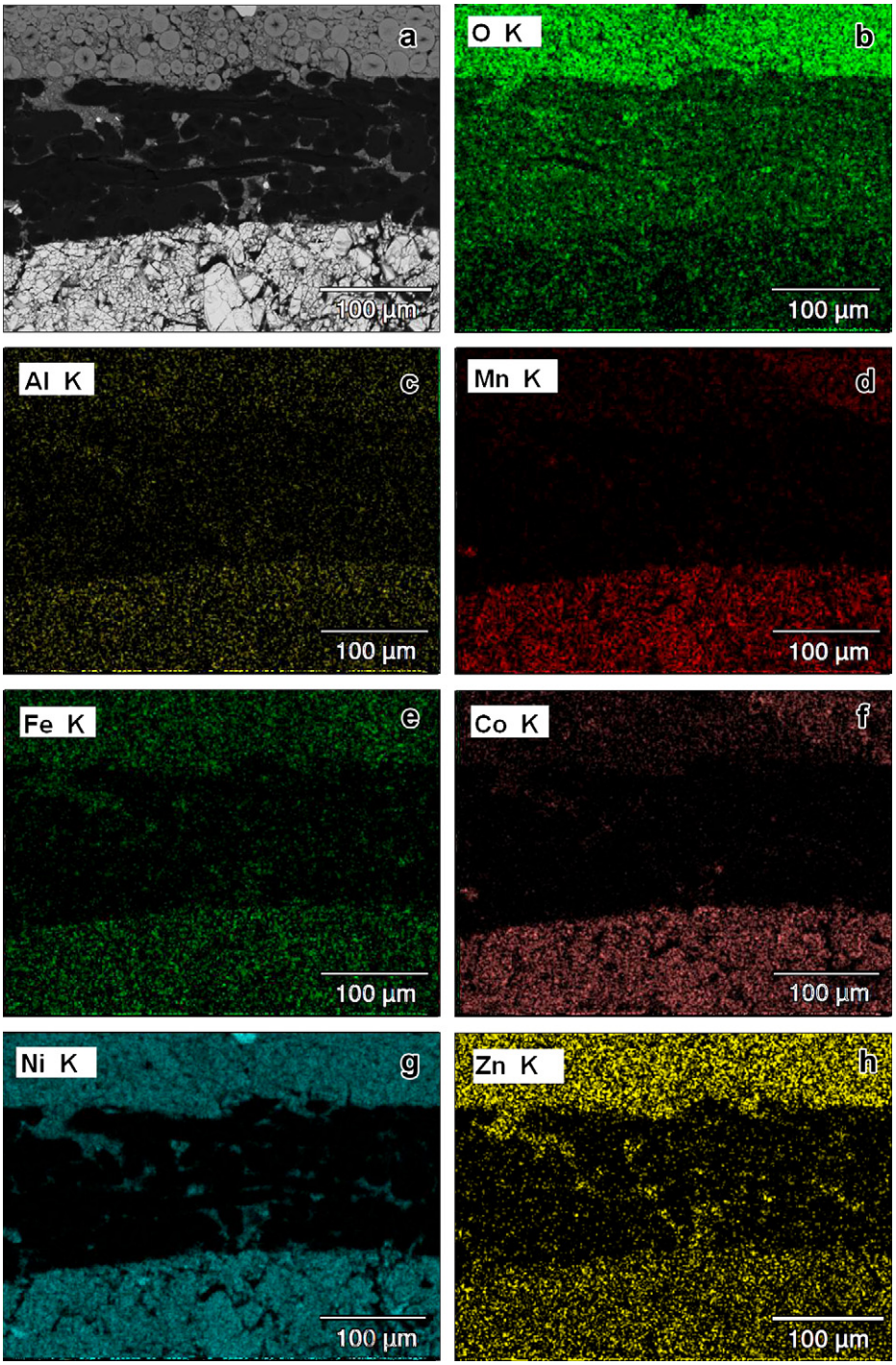

Fig. 6. SEM backscattering electron image (a) and EDS elemental mappings of O (b), Al (c), Mn (d), Fe (e), Co (f), Ni (g), and Zn (h) from the battery made from alloy #3 after 60-days storage at 60 °C. Positive electrode is at the top of the micrograph.

positive electrode, negative electrode, and separator of cells after 60-day at 60 °C storage. The concentrations of the soluble contents in the resultant solutions were studied by ICP, and the results in ppm from the group with 2% Y_2O_3 additive are shown in Table 8. The Y-distribution is different between series. In the Al-series, soluble Y can be found in both the positive and negative electrodes but not in the separator; however, the result in the Mn-series was just the opposite: Y was concentrated in the separator and not in either electrode. During battery operation, Y migrates from the positive electrode to the electrolyte, then to the surface of the negative electrode and participates in the formation of surface hydroxide together with other rare earth elements from the bulk of MH alloy [38,39]. With the continuous oxidation in the Al-series of alloys, Y can be found on the surface oxide of the negative electrode. It is somehow surprising to observe that in the Mn-series of alloys, which had the full amount of Al and less Mn, most soluble Y was found trapped in the separator together with Co. The protection against corrosion from Al can be seen in the Al-series of alloys: as the Al-content decreased, the amount of La in the separator increased. The higher degree of corrosion found in the Al-deficient

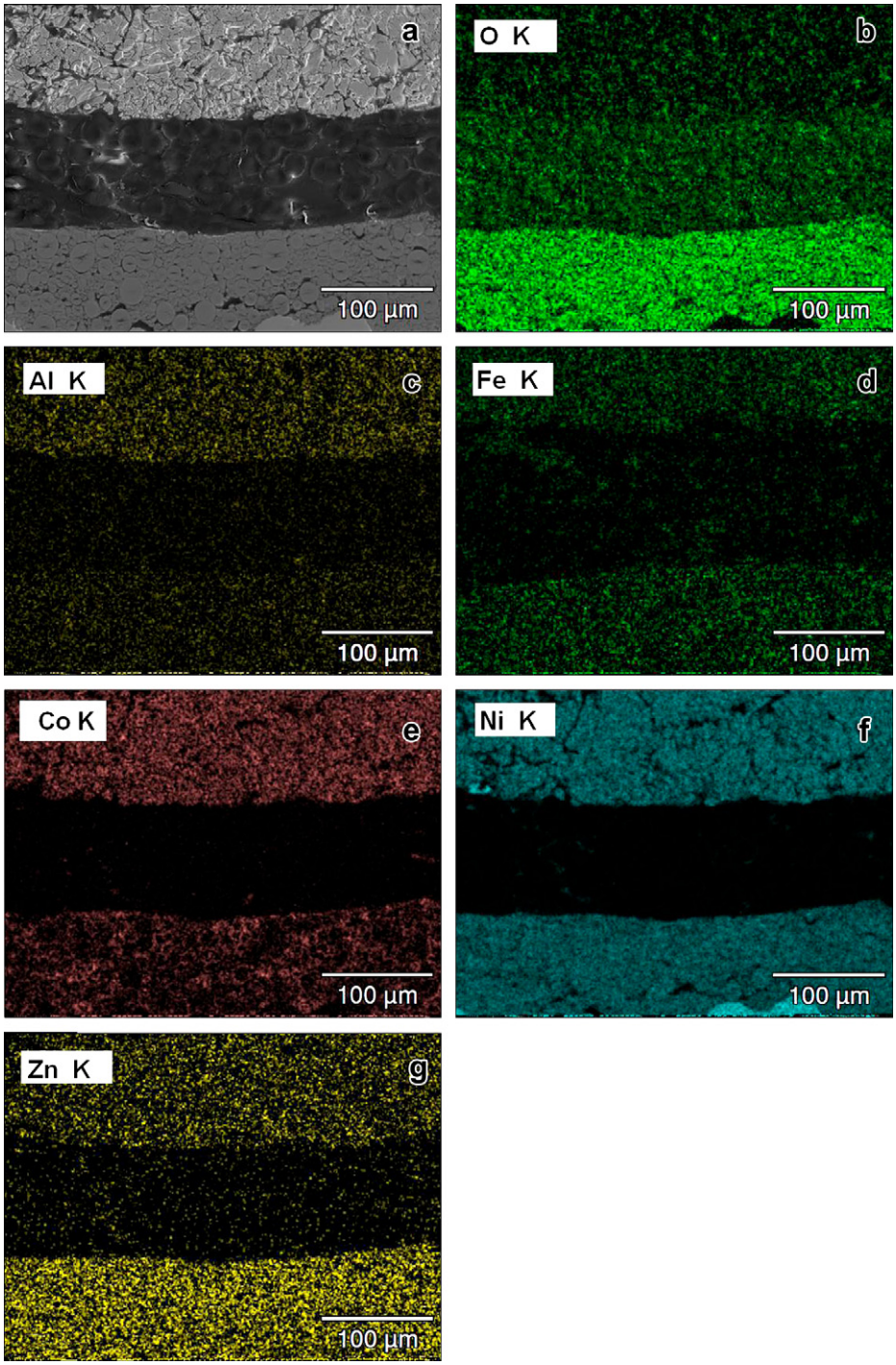

Fig. 7. SEM backscattering electron image (a) and EDS elemental mappings of O (b), Al (c), Fe (d), Co (e), Ni (f), and Zn (g) from the battery made from alloy #7 after 60-days storage at 60 °C. Positive electrode is at the bottom of the micrograph.

alloys can be correlated to the higher degree of positive electrode disintegration as seen from the higher Zn-contents in both separator and negative electrode of alloys #2, #3 and #4. In the Mn-series of alloys, the degree of positive electrode disintegration was about the same as that in alloy #1, and the soluble La-contents in both the separator and negative electrode increased as the surface area increased due to higher pulverization rate. The Fe-contents in the positive electrode, negative electrode, and separator decreased with the decrease in Al- or Mn-content in the MH alloy. With higher degree of corrosion occurring in the negative electrode, less corrosion in the exposed portion of the Ni-plated stainless steel components of the battery was found.

The cation contents in the positive electrodes from the group with 0% Y_2O_3 additive after 60-days and 60 °C storage after removing the electrolyte and soluble components by Soxhelet extraction were examined by ICP, and the results in at.% are listed in Table 9. The amounts of Mn and Al in the positive electrodes from the corrosion of the negative electrodes in some cases are very high. With the reduction in Al-content in the MH alloy, the Mn-content in the positive electrode increased and indicated a higher degree

Table 8
ICP results in ppm of soluble contents in Soxhlet extraction solutions from positive electrode, negative electrode, and separator from the cells made of 2% Y_2O_3 and various MH alloys after 60-days at 60 °C storage.

Alloy #	Pos	Pos	Pos	Pos	Neg	Neg	Neg	Neg	Neg	Neg	Sep	Sep	Sep	Sep	Sep	Sep	Sep
	Al	Fe	Y	Zn	Al	Fe	La	Mn	Y	Zn	Al	Fe	Co	La	Mn	Y	Zn
1	2.2	0.8	0.1	2.0	0.8	1.1	0.2	0.3	0.1	3.0	1.0	0.8	0.0	0.1	0.0	0.0	3.0
2	1.0	0.3	0.1	2.5	0.5	1.2	0.1	0.4	0.1	4.2	0.7	0.4	0.0	0.2	0.0	0.0	4.1
3	0.4	0.3	0.1	2.4	0.2	0.8	0.2	0.6	0.1	5.2	0.2	0.3	0.0	0.4	0.1	0.0	5.2
4	0.0	0.1	0.1	2.2	0.0	0.7	0.2	0.5	0.1	6.1	0.0	0.1	0.0	0.6	0.2	0.0	5.8
5	1.4	0.4	0.1	2.0	0.7	0.8	0.2	0.4	0.1	4.5	1.0	0.4	0.3	0.5	0.4	0.2	3.3
6	1.8	0.4	0.0	2.1	0.1	0.9	0.3	0.2	0.0	3.9	0.9	0.1	0.5	0.6	0.2	0.3	3.2
7	2.1	0.2	0.0	1.9	0.3	0.2	0.4	0.0	0.0	2.8	0.8	0.0	0.5	0.8	0.0	0.4	3.0

of corrosion in the MH alloy. As the Mn-content in the MH alloy reduced, the La- and Al-contents in the positive electrode increased and corresponded well with the higher pulverization rate of the Mn-lean alloys during cycling. The observation of the Fe-content in the positive electrode is in agreement with the result regarding the soluble Fe-content shown in Table 8. In both series, the Fe-corrosion is reduced with the reduction in either Al- or Mn-content in the MH alloys.

In order to compare the pulverization rates of various MH alloys, BEI micrographs of the negative electrodes from the cells in the first group (0% Y_2O_3 additive) are shown in Fig. 8. As seen from the evolution of the micrographs, alloy #1 with the full amounts of Mn and Al showed the largest average particle size. With the reduction in either Al (alloys #2–4) or Mn (alloys #5–7), the average particle size became smaller. The pulverization in the Mn-reduction series (alloys #5–7) was more severe than that in the Al-reduction series (alloys #2–4).

3.6. Long-term storage

Some batteries were charged at 0.1C rate for 16 h and then kept at room temperature. Both OCVs and impedances were measured and recorded at the end of 6-month and 293-day periods. The data are listed in the last four columns in Table 6. The OCVs and impedances after 6-month storage are plotted in Fig. 9a and b, respectively. In the Al-series, the OCV increased as the Al-content was decreased to 67% of the base alloy and then remained about the same with further reductions in Al-content. In the Mn-series, the OCV increased monotonically as the Mn-content decreased. In general, the Mn-series alloys had higher OCVs than those in Al-series. In both series, cells with the 2% Y_2O_3 addition showed higher OCVs. The impedance increased with the reduction in Al-content and increased slightly followed by decreases with the reduction in Mn-content. Addition of Y_2O_3 was beneficial for lowering the impedances in both series.

The evolutions of OCV with the reduction in Al and Mn for the 6-month and 293-day testing period were very similar. The Mn-series alloys had higher OCVs than those in Al-series. In both series, addition of Y_2O_3 promoted higher values of OCV after 293-day storage. The trend of impedance change with changes in composition for the 293-day storage period was identical to that of the 6-month storage period. Y_2O_3 was also beneficial in lowering the impedance in this case.

Table 9
ICP results of cation contents (at. %) in the positive electrode after Soxhlet extraction removing electrolyte and soluble contents from cells made from 0% Y_2O_3 and various MH alloys after 60-days at 60 °C storage.

Alloy #	Ni	Co	Zn	Mn	Al	La	Fe
1	84.98	7.24	6.30	0.58	0.56	0.003	0.33
2	85.36	7.24	6.03	0.63	0.48	0.002	0.26
3	85.07	7.14	6.06	1.23	0.40	0.003	0.11
4	85.79	6.54	6.28	1.28	0.00	0.008	0.09
5	85.64	7.08	5.85	0.54	0.69	0.018	0.17
6	86.04	7.18	5.87	0.05	0.72	0.020	0.12
7	85.90	7.04	6.19	0.01	0.78	0.020	0.08

4. Discussion

From data shown above, the addition of Y_2O_3 in the positive electrode raised the OCV, resulting in reductions in both reversible capacity loss and impedance during long period storage, but had little effect on irreversible capacity loss. Therefore, while the preliminary finding suggests that the OCV, reversible capacity loss, and impedance are more related to the positive electrode, the main cause for the irreversible capacity loss during storage is not. An earlier cyclic voltammogram study of Y_2O_3 addition also indicated a suppression of the oxygen evolution pressure and an increase in the charge efficiency at high-temperature [40]. During storage, Al, Mn, and Fe dissolve in the KOH solution, migrate, and deposit on the surface of $Ni(OH)_2$, which lowers the oxidation evolution potential and causes an incomplete charging of $Ni(OH)_2$. The addition of Y_2O_3 should overcome this problem and bring down the irreversible capacity loss, which was not seen here. Another function of Y_2O_3 is to form a protective layer on the MH alloy surface to slow down the oxidation process [38]. The improvement in corrosion resistance by incorporating Y_2O_3 can reduce the amount of Mn leached out, and thus reduce the shuttling effect and reduce the reversible capacity loss of the cell. Cells from Al-series had better charge recovery (less irreversible loss) than those from Mn-series, which indicates that a proper amount of Mn is very important to keep irreversible loss at a low level. Added Mn in the alloy formula can reduce the PCT hysteresis [41] and consequently reduce the pulverization rate and extend the cycle life of the negative electrode [42]. Pulverization has been identified to be the main cause of the capacity degradation [43].

Comparing long-term storage data from the Al- and Mn-series of alloys, the former had both lower OCVs and larger impedances. The Al-series of alloys had a larger unit cell volume, resulting in lower PCT plateau pressures that contributed to lower OCVs from the onset. The Al-series of alloys also were more prone to oxidation/passivation due to the reduction in Al-content as confirmed by the ICP analysis of the electrode after charge retention experiment. This is in total agreement with previous findings of Al's contribution to the corrosion resistance of the MH alloys [27,44,45].

The effectiveness of the 60 °C accelerated charge retention scheme is verified by Table 10, which lists all the correlation coefficients (R^2) among the measured battery properties listed in Table 5. A positive (negative) correlation coefficient indicates a positive (negative) correlation. The correlations to reversible capacity loss are also listed in the same table. From the table, a strong correlation between the impedance measured by the accelerated scheme (60 °C

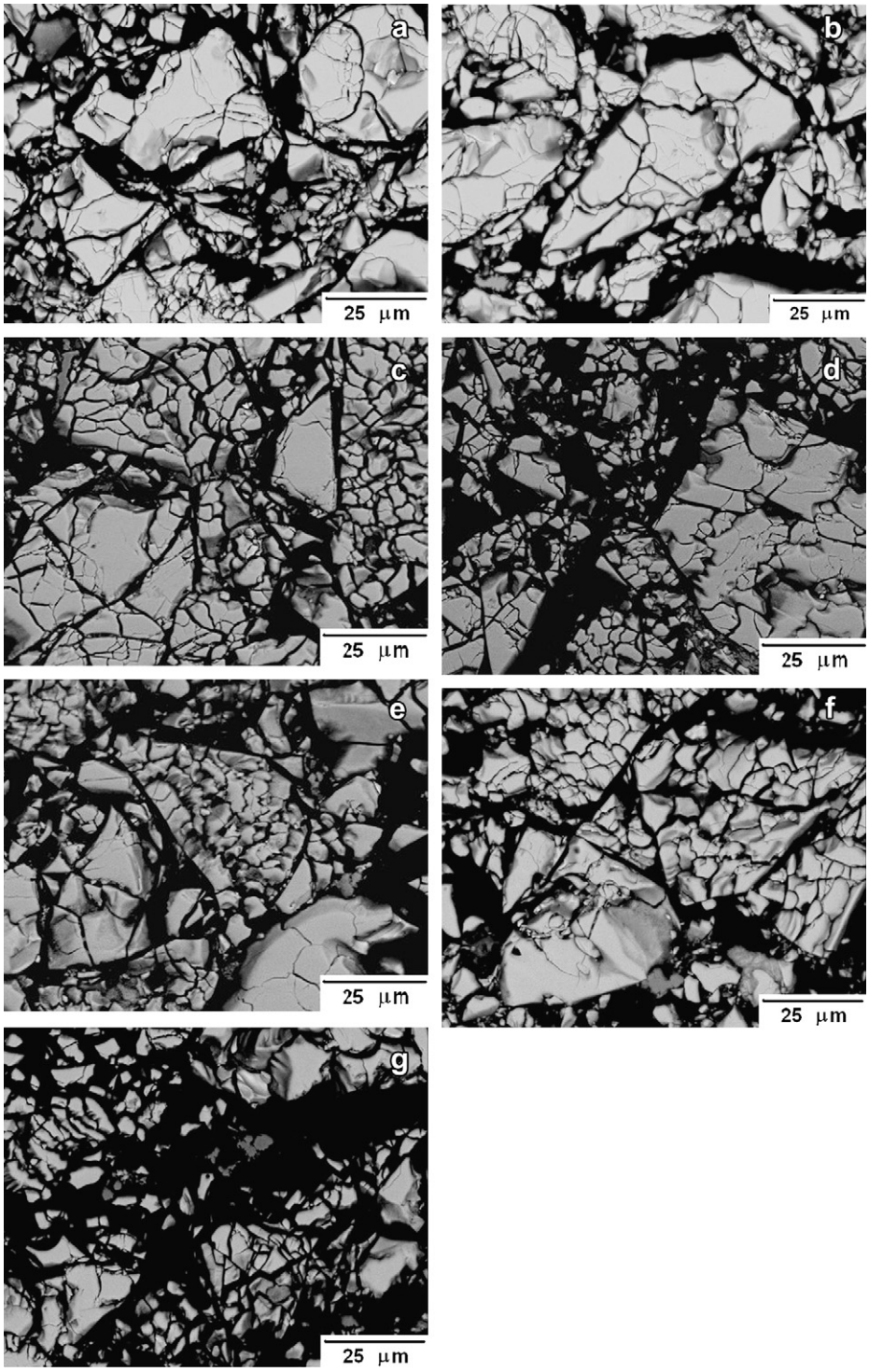

Fig. 8. SEM backscattering electron images of the negative electrode from batteries made with alloys #1 (a), #2 (b), #3 (c), #4 (d), #5 (e), #6 (f), and #7 (g) after 60-days storage at 60 °C.

for 60-days) and same quantity for long period storage (6-months and 293-days) is seen. The charge retention measured at 60 °C had a better correlation to the OCV measured at long period storage when compared to those from irreversible (charge recovery) and reversible capacity losses. Therefore, charge retention is a better way to predict OCV after a long period of storage. Combining impedance and charge retention results, the accelerated charge retention method is a valid tool to use in predicting battery characteristic changes after a long period of storage.

A closer look at the evolution of OCV vs. storage period is discussed next. Data from the first group with 0% Y_2O_3 additive are plotted in Fig. 10a. Evolutions from the other two groups with 2% and 4% Y_2O_3 are similar. It should be noted that the initial OCVs were subtracted by 0.12 V in order to be compared with other series in the graph. From this graph, it is obvious that the trend of OCVs after long period room temperature storage followed the same trend as the initial OCVs ($R^2 = 0.88$) did but was very different from that of the 60-day at 60 °C data ($R^2 = 0.00$). The initial OCV before

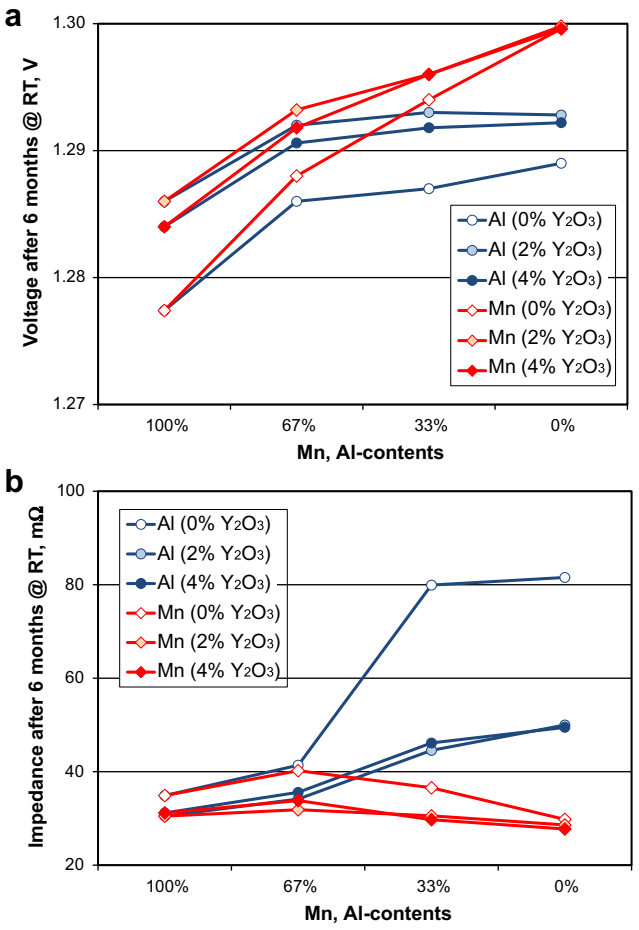

Fig. 9. The plots of open-circuit voltage (a) and impedance (b) of batteries after 6-months storage at room temperature.

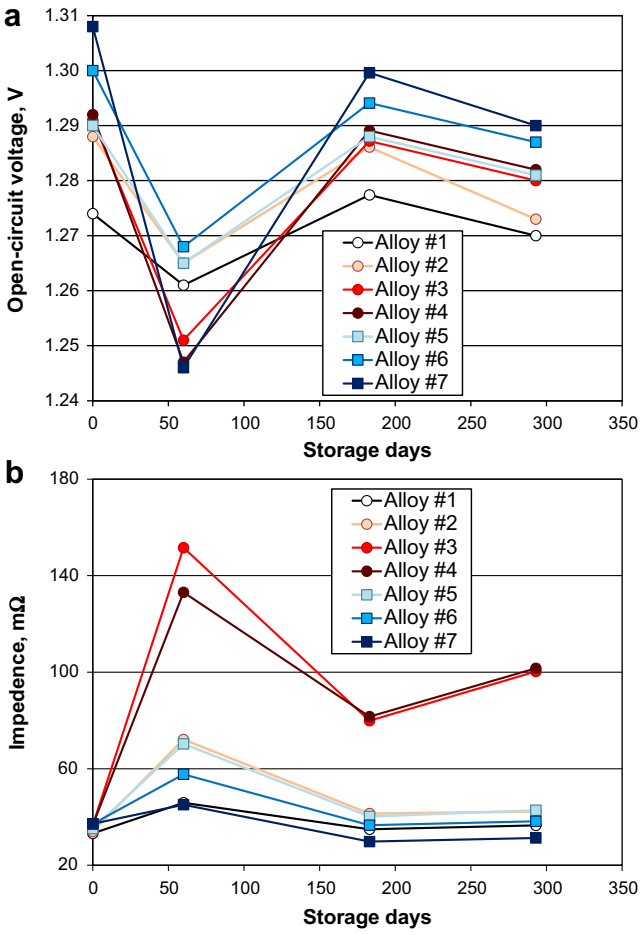

Fig. 10. The evolutions of open-circuit voltage (a) and impedance (b) with storage time for cells in the first group (no Y_2O_3). The 60-days data were taken from 60 °C while others were from room temperature. The initial OCVs have been deducted by 0.12 V in order to fit into the same graph.

storage is dominated by the PCT plateau pressure through the Nernst equation [46,47].

$$V(\text{vs.Hg/HgO}) = -0.932 - 0.0296(\log p(\text{H}_2))$$

The R^2 values between initial OCVs and MH alloy plateau pressures were 0.70, 0.62, and 0.74, for groups with 0, 2, and 4% Y_2O_3 additives, respectively. While both the initial and room temperature storage OCVs correlated well with the MH alloy plateau pressure, the 60 °C storage OCV seems to be more related to the oxidation resistance of the alloy.

The evolution of impedance vs. storage time was more coherent than that of OCV discussed above. A representative figure using data from the first group with 0% Y_2O_3 additive is shown in Fig. 10b. The other two groups with 2% and 4% Y_2O_3 also showed similar trends. The high-temperature accelerated the aging process. From the increase in impedance in alloys #3 and #4, the storage at 60 °C for 60-days was estimated to be equivalent to 600-days of storage at room temperature.

Table 10
Correlation coefficients (R^2) among the measured battery properties. A positive (negative) correlation coefficient indicates a positive (negative) correlation. The numbers in bold indicate major significance.

	Imp, 60-days, 60 °C	Ch. Ret., 60-days, 60 °C	Ch. Rec., 60-days, 60 °C	Rev. loss 60-days, 60 °C	OCV, 6-months	Imp, 6-months	OCV, 293-days	Imp, 293-days
OCV, 60-day60-days, 60 °C	−0.05	0.00	−0.02	0.00	−0.04	−0.10	0.00	−0.12
Imp, 60-day60-days, 60 °C		−0.08	+0.03	+0.14	−0.07	**+0.95**	−0.03	**+0.94**
Ch. Ret., 60-day60-days, 60 °C			**+0.54**	**−0.98**	−0.39	−0.04	**−0.50**	−0.05
Ch. Rec., 60-day60-days, 60 °C				−0.39	**−0.64**	+0.07	**−0.62**	+0.06
Rev. Loss, 60-day60-days, 60 °C					+0.29	+0.09	+0.40	+0.10
OCV, 6-months						−0.07	**+0.92**	−0.06
Imp, 6 months							−0.04	**+1.00**
OCV, 293days								−0.03

5. Summary

Reductions of Al and Mn in the MH alloy composition both generated the following results:

- No change in the uniformity of the micro-structure.
- Reduction in unit cell volume and crystallite size, and c/a ratio.
- No change in ΔH and a decrease in ΔS.
- Increase in gaseous phase hydrogen storage, equilibrium plateau pressure, and PCT hysteresis.
- Reduction in corrosion of the exposed portion of the Ni-plated stainless steel components in the cell.
- Increase in initial OCV and impedance.
- Decrease in OCV and charge retention, increase in irreversible capacity loss, and reduction in the oxide deposits trapped in the separator after storage for 60-days at 60 °C.
- Decrease in OCV after long period storage at room temperature.

Compared to the Al-reduction series, the Mn-reduction series showed the following:

- Higher corrosion resistance to KOH.
- Higher degree of pulverization in the MH alloy.
- Higher concentration of Y was found in the separator.
- Higher initial OCV and impedance.
- Higher OCV, smaller impedance increase, lower charge recovery, and less $Ni(OH)_2$ decomposition after storage for 60-days at 60 °C.
- Higher OCV and lower impedance after long period storage.

In addition, adding Y_2O_3 in the positive electrode contributed to the following

- Improvement in MH alloy corrosion resistance.
- Increase in initial and long period storage OCVs.
- Decrease in both the initial impedance and changes after 60 °C and long period storage OCVs.
- Increase in charge retention after storage at 60 °C.

Lastly, the acceleration of charge retention experiment performed at 60 °C was found to be valid. Charge retention and impedance measured from the accelerated scheme could be correlated to the open-circuit voltage and impedance after long-term storage, respectively.

Acknowledgement

Authors are sincerely grateful to T. Ouchi (sample preparation and XRD analysis), S. Cronogue (PCT measurement), R. Blackenship (ICP analysis), and J. Nei (discussion).

References

[1] M.M. Moorthi, Proceedings of Telecommunications Energy Conference (2006) Article available online: http://www.michigangreen.org/energy-news/Publication.pdf.
[2] H. Teraoka, Proceedings of Batteries, France, Nice, 2007, Sep. 26–28, Article available from: http://www.eneloop.info/fileadmin/EDITORS/ENELOOP/ARTICLES/Teraoka_Article_EN.pdf.
[3] M. Zelinsky, J. Koch, M. Fetcenko, Proceedings of Battcon 2010 International Stationary Conference. Article available online: http://www.energyconversiondevices.com/pdf/ZelinskyPaper2010Final_12.pdf.
[4] S. Yasuoka, Y. Magari, T. Murata, T. Tanaka, J. Ishida, H. Nakamura, T. Nohma, M. Kahara, Y. Baba, H. Teraoka, J. Power Sources 156 (2006) 662.
[5] S. Vorkoetter. In Review: Pre-charged (Low Self-discharge) Rechargeable Battery Comparison. Article available online: http://www.stefanv.com/electronics/low_self_discharge.html
[6] N. Furukawa, J. Power Sources 51 (1994) 45.
[7] M. Ikpma, Y. Hoshina, I. Matsumoto, C. Iwakura, J. Electrochem. Soc. 143 (1996) 1904.
[8] P. Leblanc, P. Blanchard, S. Senyarich, J. Electrochem. Soc. 145 (1998) 844.
[9] P. Kritzer, J. Power Sources 137 (2004) 317.
[10] K. Shinyama, Y. Harada, R. Maeda, H. Nakamura, S. Matsuta, T. Nohma, I. Yonezu, Res. Chem. Intermed 32 (2006) 447.
[11] F. Meli, T. Sakai, A. Züttle, L. Schlapbach, J. Alloys Compd. 221 (1995) 284.
[12] K. Shinyama, T. Nohuna, M. Takee, K. Ishiwa, J. Power Sources 141 (2005) 193.
[13] P. Bäuerlein, C. Antonius, J. Löffler, J. Kümpers, J. Power Sources 176 (2008) 547.
[14] X. Li, Y. Song, L. Wang, T. Xia, S. Li, Int. J. Hydrogen Energ. 35 (2010) 3798.
[15] K. Young, T. Ouchi, J. Koch, M.A. Fetcenko, J. Alloys Compd. 510 (2012) 97.
[16] K. Young, T. Ouchi, B. Huang, M.A. Fetcenko, J. Alloys Compd. 511 (2012) 242.
[17] K. Shinyama, Y. Magari, H. Akita, K. Kumagae, H. Nakamura, S. Matsuta, T. Nohma, M. Takee, K. Ishiwa, J. Power Sources 143 (2005) 265.
[18] C. Iwakura, Y. Kajiya, H. Yoneyama, T. Sakai, K. Oguro, H. Ishikawa, J. Electrochem. Soc. 136 (1989) 1351.
[19] J.H. Lee, K.Y. Lee, J.Y. Lee, J. Alloys Compd. 232 (1996) 197.
[20] X. Yang, B. Liaw, J. Electrochem. Soc. 151 (2004) A137.
[21] C. Wang, M. Marrero-Rivera, D.A. Serafini, J.H. Baricuatro, M.P. Soriaga, S. Srinivasan, Int. J. Hydrogen Energ. 31 (2006) 603.
[22] D. Singh, T. Wu, M. Wendling, P. Bendale, J. Ware, D. Ritter, L. Zhang, Mat. Res. Soc. Symp. Proc. 496 (1998) 25.
[23] X. Zhang, Z. Gong, S. Zhao, M. Geng, Y. Wang, D.O. Northwood, J. Power Sources 175 (2008) 630.
[24] C.S. Wang, M. Marrero-Rivera, J.H. Baricuatro, M.P. Soriaga, D. Serafini, S. Srinivasan, J. Appl. Electrochem. 33 (2003) 325.
[25] X. Li, B. Xia, J. Alloys Compd. 391 (2005) 190.
[26] T. Sakai, H. Miyamura, N. Kuriyama, A. Kato, K. Oguro, H. Ishikawa, C. Isakura, J. Less-Comm. Met. 159 (1990) 127.
[27] K. Young, M.A. Fetcenko, T. Ouchi, F. Li, J. Koch, J. Alloys Compd. 464 (2008) 238.
[28] K. Young, M.A. Fetcenko, J. Koch, K. Morii, T. Shimizu, J. Alloys Compd. 486 (2009) 559.
[29] J.M. Joubert, R. Černỳ, M. Latriche, A. Percheron-Guegan, K. Yvon, J. Allp. Crystallogr. 31 (1998) 327.
[30] P.A. Georgiev, J. Liu, D.K. Ross, K.H. Andersen, A. Otto, J. Alloys Compd. 349 (2003) 325.
[31] Y. Osumi, H. Suzuki, A. Kato, K. Oguro, S. Kawai, M. Kaneko, J. Less-Comm. Met. 89 (1983) 287.
[32] Y. Osumi, in: Agune Technology Center, new ed. Japan, Tokyo, 1999, p. 46.
[33] K. Young, T. Ouchi, M.A. Fetcenko, J. Alloys Compd. 480 (2009) 428.
[34] K. Young, T. Ouchi, W. Mays, B. Reichman, M.A. Fetcenko, J. Alloys Compd. 480 (2009) 434.
[35] K. Young, T. Ouchi, M.A. Fetcenko, J. Alloys Compd. 480 (2009) 440.
[36] L. Schlapbach, A. Züttle, Nature 414 (2001) 353.
[37] K. Young, T. Ouchi, J. Koch, M.A. Fetcenko, J. Alloys Compd. 477 (2009) 749.
[38] H. Kaiya, T. Ookawa, J. Alloys Compd. 231 (1995) 598.
[39] F. Maurel, P. Leblanc, B. Knosp, M. Backhaus-Ricoult, J. Alloys Compd. 309 (2000) 88.
[40] X. Mi, M. Ye, J. Yan, J. Wei, X. Gao, J. Rare Earths 22 (2004) 422.
[41] M.N. Mungole, R. Balasubramaniam, K.N. Rai, Int. J. Hydrogen Energ. 24 (1999) 467.
[42] T. Sakai, K. Oguro, H. Miyamura, N. Kuriyama, A. Kato, H. Ishikawa, C. Iwakura, J. Less-Comm. Met. 161 (1990) 193.
[43] P. Leblanc, C. Jordy, B. Knosp, Ph. Blanchard, J. Electrochem. Soc. 145 (1998) 860.
[44] J.J.G. Willems, K.H.J. Buschow, J. Less-Comm. Met. 129 (1987) 13.
[45] F. Meli, L. Schlapbach, J. Less-Comm. Met. 172–174 (1991) 1252.
[46] X.B. Zhang, D.Z. Sun, W.Y. Yin, Y.J. Chai, M.S. Zhao, Electrochim. Acta 50 (2005) 2911.
[47] S. Bliznakov, E. Lefterova, N. Dimitrov, Int. J. Hydrogen Energ. 33 (2008) 5789.